IEEE Access
Multidisciplinary | Rapid Review | Open Access Journal

Received 27 December 2022, accepted 22 January 2023, date of publication 25 January 2023, date of current version 1 February 2023.

Digital Object Identifier 10.1109/ACCESS.2023.3239956

RESEARCH ARTICLE

Computed Tomography Reconstruction Using Only One Projection Angle

FAWAZ HJOUJ AND MOHAMED SOUFIANE JOUINI
Department of Mathematics, Khalifa University, Abu Dhabi, United Arab Emirates
Corresponding author: Fawaz Hjouj (fawaz.hjouj@ku.ac.ae)

ABSTRACT Let F represent a digitized version of an image $f(x, y)$. Assume that the image fits inside a rectangular region and this region is subdivided into $M \times N$ squares. We call these squares the shifted box functions. Thus $f(x, y)$ is approximated by $M \times N$ matrix F. This paper proofs that F can be recovered exactly and uniquely from the Radon transform of f using only one selected view angle with a well selected family of MN lines. The paper also proposes a precise method for computing the Radon transform of an image. The approach can be categorized as an algebraic reconstruction, but it is merely a theoretical contribution for the field of limited data tomography.

INDEX TERMS Algebraic reconstruction, radon transform, tomography, limited data tomography.

I. INTRODUCTION

In this paper, we propose a new algebraic reconstruction algorithm for tomography using only one selected view angle of projection with a selected family of projection lines. Our proposed approach is a nontraditional algebraic approach, recursive, but a theoretical solution.

Tomography is defined as the process of recovering an object from measurements that are line integrals of that object at a known complete set of view angles. In 1917 Radon, [1], showed that it is possible to recover a suitably regular real valued function f from the set of all projections $f^{\vee}(p, \varphi)$ for angles of projections φ, and all lines $p = x\cos\varphi + y\,sin\varphi$. Radon's work found applications in the field of computed tomography [2], [3], [4], [5]. In this context, $f(x, y)$ corresponds to the density of tissue at a point (x, y) in some plane slice through a human body and the Radon transform is a measure of the logarithm of the absorption of an x-ray beam that passes through the body along the line L. In addition to its use in the medical imaging; tomography has been successfully applied in various applications such as Digital Rock Physics, for instance [6], [7]. Additionally, image registration techniques utilize the integral transforms approach including the Radon transform, and others. Different approaches are proposed to recover spatial transformations relating two images using their Radon transforms [8], [9], [10]. Another major approach related to Radon transform uses invariant pattern recognition [11], [12], [13].

In the field of tomography, there are several categories of reconstruction algorithms for approximating the inversion of Radon transform [2]; this includes: signal space convolution and frequency space filtering in which the filtered back projection is one possible approach; series methods and orthogonal functions; Fourier methods, that comes from the Fourier slice theorem; algebraic-iterative methods and others. The Algebraic Reconstruction Technique (ART), Simultaneous Iterative Reconstruction Technique (SIRT), and, the Simultaneous Algebraic Reconstruction Technique (SART); all were developed for tomography applications [14], [15], [16], [17], [18]. In fact, the ART methods are based on Kaczmarz' method [19], [20]. Modern approaches for the low-dose computed tomography problem and denoising includes what is known today as "the machine learning for image reconstruction" [21], [22], [23], [24], such as batch gradient descent, stochastic gradient descent, and many others.

The original inversion formula given by Radon [1], is valid when f is continuous with compact support and that the projections $f^{\vee}(p, \varphi)$ are given for all lines-infinite set of projections, not a discrete one. In the traditional tomography, a full range of projections are available. These projections are given over 0 to π with a fine uniformly spaced radial

The associate editor coordinating the review of this manuscript and approving it for publication was Yiming Tang.

values defining the lines of integration. The term limited set of Radon projections takes different forms due to different applications or mathematical assumptions associated with it. Examples of variations of mathematical assumptions can include, only few projections are available, or projections are available on a limited range of angles, or other conditions. The problem of recovering a function $f(x, y)$ from a limited set of Radon projections has been dealt with in the mathematical and engineering literatures, for instance, [25], [26], [27], [28], [29], [30], [31], [32], [33], [34], [35], [36], [37], [38], [39], [40], [41]. Examples of different approaches include interpolating the missing views such as [25], spectrum analysis [24], statistical iterative methods [27]. A common approach is the theory of using different moments to recover the function, [28], [29], [30].

Another major approach is the algebraic reconstruction methods which are optimization-based iterative methods to compensate for the imaging artifacts induced by the limited projections [31]. Algebraic reconstruction approaches, such as [14], [15], [16], [17], [18], and [31], perform better than the traditional filtered-back projection method, at the expense of computational cost. To better constrain the solution, compressive sensing techniques [32], [33] have been applied to promote sparsity in reconstructions. As said, the Machine learning for image reconstruction [21], [22], [23], [24], [34], [35], [36], [37] provide an alternative. These studies are essentially focused on image processing with pre-trained deep networks, either to in-paint sinogram images [34], [35], or to correct artifacts in reconstructed images [36], [37].

In this paper, we present a new theoretical algorithm for tomography using only one selected view angle of projection with a well selected family of MN lines. In fact, we propose a direct algebraic reconstruction solution by recovering the image piece by piece, for example column by column. In doing so, we solve small linear systems recursively. We use the unit box function to represent each pixel of the image which allows us to use a closed form formula for the Radon transform of the box; so that the system matrix is exact. The result of this work is a pure computation and may not be applied for a real tomography problem. The work is organized as follows: In section II, we give background material regarding the Radon transform, image representation, and a review of the algebraic reconstruction method. In section III, we present our theorem for algebraic reconstruction from one view angle of projection as well as a demonstration. A numerical evaluation is presented in section IV. Finally, the conclusion is written in section V.

II. BACKGROUND MATERIAL

This section presents a review of three mathematical tools and notation that will be used in this work. These tools are: a review of the Radon transform, image representation using the box function, and a review of the algebraic reconstruction method.

Let (x, y) designate the coordinates of points in the plane and consider a function f defined on some domain D of R^2. Consider the line L in the plane whose equation in the normal form is given by

$$L = \{(x, y) : x\cos\varphi + y\sin\varphi = p\} \tag{1}$$

One way to write the Radon transform of f along the line L is:

$$f^{\vee}(p, \varphi) = \int_{-\infty}^{\infty} f(p\cos\varphi - t\sin\varphi, p\sin\varphi + t\cos\varphi)dt \tag{2}$$

We refer to $f^{\vee}(p, \varphi)$ or $f_{\varphi}^{\vee}(p)$ as the Radon projection of f. More precisely, the term Radon projection, in this work, means a single non-negative number equals to the line integral of f along one line specified by the pair (p, φ).

Among the basic properties of Radon transform is the shifting property that is relevant to our discussion: If g is obtained from f by the real translation parameters x_0, y_0 so that

$$\begin{aligned} g(x, y) &= f(x - x_0, y - y_0), \text{ then :} \\ g^{\vee}(p, \theta) &= f^{\vee}[p - (x_0\cos\theta + y_0\sin\theta), \theta] \end{aligned} \tag{3}$$

Another common tool that we need is the "Box Function",

$$B(x, y) := 1 \quad \text{for } 0 < x < 1,\ 0 < y < 1 \text{ and zero otherwise,} \tag{4}$$

as shown in Fig 1a. By direct calculations [2], we obtain the analytical form of the Radon transform of this function

$$B^{\vee}(p, \varphi) = \begin{cases} \dfrac{p}{\sin\varphi\cos\varphi}, & 0 < p < \sin\varphi \\ \dfrac{1}{\cos\varphi}, & \sin\varphi \le p \le \cos\varphi \\ \dfrac{\sin\varphi + \cos\varphi - p}{\sin\varphi\cos\varphi}, & \cos\varphi < p < \sin\varphi + \cos\varphi \end{cases} \tag{5}$$

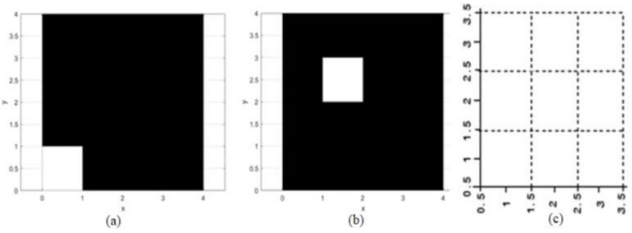

FIGURE 1. (a): The Box function in (4), (b) a shifted box in (6). (c) spatial coordinate system (x,y), as well as the pixel indexing system.

In this paper, we will be working with a function that is made of shifted box functions. Let M, N be two positive integers and let

$$\begin{aligned} B_{ij}(x, y) = B[x - (j - 1), y - (M - i)], \text{ where} \\ i = 1, \ldots, M, \text{ and } j = 1, \ldots, N \end{aligned} \tag{6}$$

represents a shifted box function, as shown in Fig. 1b.

Define the function,

$$f(x,y) := \sum_{i=1}^{M}\sum_{j=1}^{N} F_{ij}.B_{ij}(x,y) \tag{7}$$

where F_{ij} are real positive values. In this way, the function f is a non-negative real valued function defined on the compact support $[0,M]\times[0,N]$ that is subdivided into MN boxes. We work with both spatial coordinate system (x, y), as well as the pixel indexing system (i, j), as suggested in Fig 1c.

Let $f^{\vee}(p,\varphi)$ be the Radon transform of f in (7), using (3) and (5) to obtain:

$$\begin{aligned} & f^{\vee}(p,\varphi) \\ &= \sum_{i=1}^{M}\sum_{j=1}^{N} F_{ij}.B_{ij}^{\vee}(p,\varphi) \\ &= \sum_{i=1}^{M}\sum_{j=1}^{N} F_{ij}.B^{\vee}[p-\{(j-1)\,cos\varphi+(M-i)\,sin\varphi\},\varphi] \end{aligned} \tag{8}$$

One can always map a given $M\times N$ image to f with F_{ij} being the grey levels of the image. Exact calculations can then be performed.

Finally, we review the basics of the algebraic reconstruction approach. Algebraic methods basically work with a linear system $A\boldsymbol{x}=\boldsymbol{b}$ that is generated from the raw projections. Given k views of an image at the angles $\varphi_1,\varphi_2,\ldots,\varphi_k$. The system is built so that the entries of matrix A are the Radon transforms of boxes $B_{ij}^{\vee}(p,\varphi)$. These entries are nonzero only if the line of projection passed through the pixel (i,j), as in Fig. 2. Thus, matrix A is a sparse matrix. The column vector $\boldsymbol{x}$ is an $MN\times 1$ column of the MN unknows $\{F_{ij}\}$, written as:

$$\boldsymbol{x}=[F_{11},F_{12},\ldots F_{1N},F_{21},F_{22}\ldots,F_{2N},F_{M1},F_{M2}\ldots,F_{MN}]^T \tag{9}$$

where T is for the transpose. Assuming m projections (lines) for each angle, then we have mk equations. In this way, the size of matrix A is $(mk\times MN)$. The vector $\boldsymbol{b}$ is an $(mk\times 1)$ column vector of the measurement $f^{\vee}(p,\varphi)$. Every single choice of a fixed angle φ at a fixed radial value p generates one equation for the above system. A typical equation of this system would be of the form:

$$\begin{aligned} & B_{11}^{\vee}(p,\varphi).F_{11}+\cdots+B_{1N}^{\vee}(p,\varphi).F_{1N}+B_{21}^{\vee}(p,\varphi).F_{21} \\ & \quad +\cdots+B_{2N}^{\vee}(p,\varphi).F_{2N} \\ & \quad +\ldots+B_{M1}^{\vee}(p,\varphi).F_{M1}+\cdots+B_{MN}^{\vee}(p,\varphi).F_{MN} \\ & \quad = f^{\vee}(p,\varphi) \end{aligned} \tag{10}$$

In matrix from, we have,

$$\begin{bmatrix} B_{11}^{\vee}(p,\varphi) & \ldots & B_{1N}^{\vee}(p,\varphi) & \ldots & B_{M1}^{\vee}(p,\varphi) & \cdots & B_{MN}^{\vee}(p,\varphi) \\ \vdots & . & . & . & . & \ddots & \vdots \\ . & . & . & . & . & . & . \\ B_{11}^{\vee}(p,\varphi) & \ldots & B_{1N}^{\vee}(p,\varphi) & \ldots & B_{M1}^{\vee}(p,\varphi) & \ldots & B_{MN}^{\vee}(p,\varphi) \end{bmatrix} \times \begin{bmatrix} F_{11} \\ \vdots \\ F_{1N} \\ \vdots \\ F_{M1} \\ \vdots \\ F_{MN} \end{bmatrix} = \begin{bmatrix} f^{\vee}(p,\varphi) \\ \vdots \\ . \\ . \\ . \\ . \\ f^{\vee}(p,\varphi) \end{bmatrix} \tag{11}$$

Each row of the matrix A corresponds to ***a new pair*** p,φ, and each entry of $\boldsymbol{b}$ is the Radon transform at that new pair p,φ.

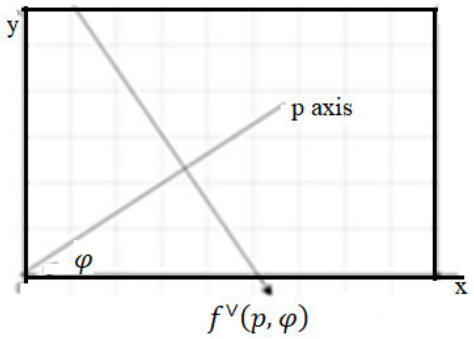

FIGURE 2. A projection for (10).

III. METHODOLOGY

A. A PROPOSITION

Let $f(x,y)$ be a non-negative real valued function such that,

(a) $f(x,y)$ is a piecewise continuous of the form $f(x,y) := \sum_{i=1}^{M}\sum_{j=1}^{N} F_{ij}.B_{ij}(x,y)$ defined in (7).
(b) In this way, the function f is defined on the compact support $[0,M]\times[0,N]$ that is subdivided into MN boxes.
(c) Let $f^{\vee}(p,\varphi)$ be the Radon transform of f. This transform is well defined and is calculated in (8).

Then, the following theorem hold.

Theorem 1: Under the above assumptions, the value of f is completely determined by $f^{\vee}(p,\varphi)$ using one angel of projection, φ_0, and a family of MN lines $p_{i,j}$ such that:

$$\begin{aligned} \varphi_0 &= \frac{\pi}{2}-\alpha;\ \text{with}\ \alpha = tan^{-1}(M),\ \text{and} \\ p_{i,j} &:= (j-1)\,cos\varphi_0+(M-i+1)\,sin\varphi_0, \\ & \quad i=1,\ldots,M,\ \text{and}\ j=1,\ldots,N \end{aligned} \tag{12}$$

The following constructive proof demonstrates an algorithm to determine f.

Proof: The approach here is an algebraic reconstruction. Consider the required family of lines (12). From (1), the line $p_{i,j}$ passes through the point $(j-1,M-i+1)$. Let us recover the first column of f by backward recursive calculations using the data $f^{\vee}\left(p_{i,1},\varphi_0\right), i = 1,\ldots,M$.

Observe that:

$$\begin{aligned}\frac{1}{sin\alpha}F_{M,1} &= f^{\vee}\left(p_{M,1},\varphi_0\right)\\ \frac{1}{sin\alpha}F_{M-1,1}+\frac{1}{sin\alpha}F_{M1} &= f^{\vee}\left(p_{M-1,1},\varphi_0\right)\\ \frac{1}{sin\alpha}F_{M-2,1}+\frac{1}{sin\alpha}F_{M-1,1}+\frac{1}{sin\alpha}F_{M1} &= f^{\vee}\left(p_{M-2,1},\varphi_0\right)\end{aligned}$$

Notice that $\frac{1}{sin\alpha}$ is the length of the segment of the line $p_{i,j}$ that lies within the box.

In general, we solve for $F_{M-I,1}$, using the equation

$$\frac{1}{sin\alpha}\sum_{i=0}^{I}F_{M-i,1}=f^{\vee}\left(p_{M-I,1},\varphi_0\right),\quad I=0,\ldots,M-1 \tag{13}$$

Fig 3, in the demonstration section, illustrates the idea with $M=N=4$, assuming one angle of projection, say φ_0, with 16 lines.

So far, we have recovered the first column of f. To recover the next column, we update the data. Let

$$g_2(x,y) := f(x,y) \ \textbf{after the first column of } f \times \textbf{has been zeroed out}. \tag{14}$$

Accordingly,

$$g_2^{\vee}(p,\varphi)=f^{\vee}(p,\varphi)-\sum_{i=1}^{M}\sum_{j=1}^{1}F_{ij}.B_{ij}^{\vee}(p,\varphi) \tag{15}$$

The first column of g_2 is now zeros. To recover the second column of g_2, which is the second column of f, we use the lines $p_{i,2}$, $i=1,2,\ldots,M$ where equation (13) is now:

$$\frac{1}{sin\alpha}\sum_{i=0}^{I}F_{M-i,2}=g_2^{\vee}\left(p_{M-I,2},\varphi_0\right),\quad I=0,\ldots,M-1 \tag{16}$$

In general, define,

$$g_J(x,y) := f(x,y) \ \textbf{after the first } (\mathrm{J}-1) \textbf{ columns of } f \times \textbf{have been zeroed out}, \quad \mathrm{J}=2,\ldots\mathrm{N}. \tag{17}$$

with

$$g_J^{\vee}(p,\varphi)=f^{\vee}(p,\varphi)-\sum_{i=1}^{M}\sum_{j=1}^{J-1}F_{ij}.B_{ij}^{\vee}(p,\varphi),\quad \mathrm{J}=2,\ldots\mathrm{N} \tag{18}$$

Thus, to recover the J^{th} column, $\mathrm{J}=2,\ldots\mathrm{N}$, perform a recursive use of

$$\frac{1}{sin\alpha}\sum_{i=0}^{I}F_{M-i,J}=g_J^{\vee}\left(p_{M-I,J},\varphi_0\right),\quad I=0,\ldots,M-1 \tag{19}$$

This completes the proof.

B. DEMONSTRATION

To illustrate the idea, as shown in Fig 3; assume that $M=N=4$, and

$$f(x,y) := \sum_{i=1}^{4}\sum_{j=1}^{4}F_{ij}.B_{ij}(x,y) \tag{20}$$

Assuming one angle of projection,

$$\varphi_0=\frac{\pi}{2}-\alpha;\ with\ \alpha=tan^{-1}(4), \tag{21}$$

and the family of 16 lines:

$$p_{i,j} := (j-1)\,cos\varphi_0+(M-i+1)sin\varphi_0,\quad i=1,2\ldots,4,\ j=1,2,\ldots,4 \tag{22}$$

The first four lines, $p_{1,1}$, $p_{2,1}$,$p_{3,1}$, and $p_{4,1}$, are shown in Fig 3a. These four lines pass through the first column of f. To recover the first column of f, apply (13) to build the following system:

$$\begin{aligned}\frac{1}{sin\alpha}F_{41} &= f^{\vee}\left(p_{4,1},\varphi_0\right)\\ \frac{1}{sin\alpha}F_{31}+\frac{1}{sin\alpha}F_{41} &= f^{\vee}\left(p_{3,1},\varphi_0\right)\\ \frac{1}{sin\alpha}F_{21}+\frac{1}{sin\alpha}F_{31}+\frac{1}{sin\alpha}F_{41} &= f^{\vee}\left(p_{2,1},\varphi_0\right)\\ \frac{1}{sin\alpha}F_{11}+\frac{1}{sin\alpha}F_{21}+\frac{1}{sin\alpha}F_{31}+\frac{1}{sin\alpha}F_{41} &= f^{\vee}\left(p_{1,1},\varphi_0\right)\end{aligned} \tag{23}$$

In this way, coulmn one is now determined. Fig 3b illustrates $g_2(x,y)$ from (14) and the four lines $p_{1,2}$, $p_{2,2}$,$p_{3,2}$, and $p_{4,2}$ that are involved in (16).

A summary of the above arguments is as follows:

1. The image in question is assumed to be of the form $f(x,y) := \sum_{i=1}^{M}\sum_{j=1}^{N}F_{ij}.B_{ij}(x,y)$ defined in (7)
2. Only one angle of projections is needed, namely, $\varphi_0=\frac{\pi}{2}-tan^{-1}(M)$
3. Recovering the J^{th} column of f requires M lines, namely,
$$p_{i,J} := (J-1)\,cos\varphi_0+(M-i+1)sin\varphi_0,\quad i=1,2\ldots,M$$
4. Thus, a total of MN Radon projections are needed: $f^{\vee}\left(p_{i,j},\varphi_0\right), i=1,\ldots M,$ and $j=1,\ldots,N$

IV. RESULTS: NUMERICAL EVALUATION

A. AN EXAMPLE OF ANALYTIC SIMULATION

Let $f(x,y)$ be an $M\times N$ image such that

$$F_{ij}=i+j \tag{24}$$

For instance, Fig 4 shows a 4×4 image of this class.

Consider $g_J^{\vee}$ from (19). For (24), we can write,

$$g_J^{\vee}\left(p_{I,J},\varphi_0\right)=\frac{1}{sin\alpha}\left[\sum_{i=I}^{M}i+[M-I+1]J\right] \tag{25}$$

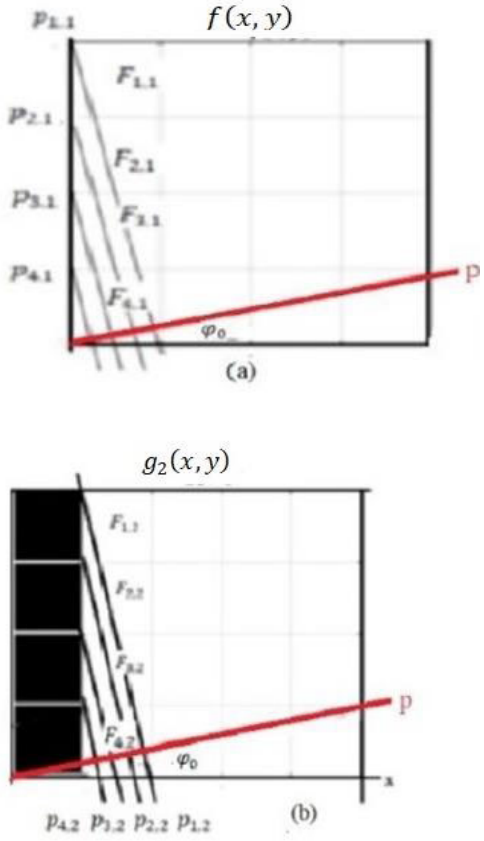

FIGURE 3. (a). $f(x, y)$ with the first set of four lines $p_{1,1}$, $p_{2,1}$, $p_{3,1}$, and $p_{4,1}$ out of 16 lines correspond to one angle of projection φ_0. (b). $g_2(x, y)$ from (14) with the second set of four lines $p_{1,2}$, $p_{2,2}$, $p_{3,2}$, and $p_{4,2}$ that are involved in (16).

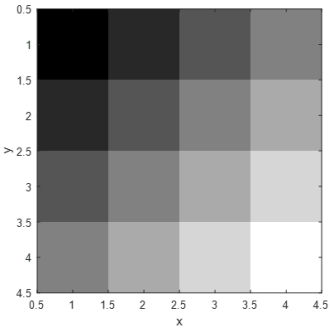

FIGURE 4. A 4 × 4 image with $F_{ij} = i + j$.

On the other hand, consider (19) and (25):

$$\frac{1}{sin\alpha}\sum_{i=0}^{I} F_{M-i,J} = g_J^{\vee}\left(p_{M-I,J}, \varphi_0\right), \quad I = 0, \ldots, M-1$$

If $I = 0$, then,

$$\begin{aligned} F_{M,J} &= sin\alpha.\left[g_J^{\vee}\left(p_{M,J}, \varphi_0\right)\right] \\ &= sin\alpha[\frac{1}{sin\alpha}(M+J)] = M+J \end{aligned} \tag{26}$$

For $I = 1, \ldots, M-1$; we use (19) to write

$$\begin{aligned} \frac{1}{sin\alpha}\sum_{i=0}^{I} F_{M-i,J} - \frac{1}{sin\alpha}\sum_{i=0}^{I-1} F_{M-i,J} \\ = g_J^{\vee}\left(p_{M-I,J}, \varphi_0\right) - g_J^{\vee}\left(p_{M-I+1,J}, \varphi_0\right). \end{aligned} \tag{27}$$

Simplify the left side of (27), and apply (25) on the right side, we obtain,

$$\begin{aligned} F_{M-I,J} &= g_J^{\vee}\left(p_{M-I,J}, \varphi_0\right) - g_J^{\vee}\left(p_{M-I+1,J}, \varphi_0\right) \\ &= \{\sum_{i=M-I}^{M} i + [M-(M-I)+1]J\} \\ &\quad - \{\sum_{i=M-I+1}^{M} i + [M-(M-I+1)+1]J\} \\ &= \{\sum_{i=M-I}^{M} i + [I+1]J\} - \{\sum_{i=M-I+1}^{M} i + IJ\} \\ &= M - I + J. \end{aligned} \tag{28}$$

From (26) and (28) we have, $F_{M-I,J} = M - I + J, I = 0, \ldots, M-1$, as expected.

B. DISCUSSION

Let us write (19) in the matrix form:

$$\frac{1}{sin\alpha}\begin{bmatrix} 1 & 0 & 0 & \ldots & 0 & 0 \\ 1 & 1 & 0 & \ldots & 0 & 0 \\ 1 & 1 & 1 & 0 & \ldots & 0 \\ \vdots & \vdots & \vdots & \vdots & \vdots & \vdots \\ 1 & 1 & 1 & \ldots & 1 & 1 \end{bmatrix}\begin{bmatrix} F_{M,J} \\ F_{M-1,J} \\ F_{M-2,J} \\ \vdots \\ \vdots \\ F_{2,J} \\ F_{1J} \end{bmatrix} = \begin{bmatrix} g_J^{\vee}\left(p_{M,J}, \varphi_0\right) \\ g_J^{\vee}\left(p_{M-1,J}, \varphi_0\right) \\ g_J^{\vee}\left(p_{M-2,J}, \varphi_0\right) \\ . \\ . \\ . \\ g_J^{\vee}\left(p_{1,J}, \varphi_0\right) \end{bmatrix} \tag{29}$$

In this way, the J^{th} column of the desired image, (flipped upside down), is recovered by solving (29).

To verify the overall effectiveness of the proposed method, experiments were performed on different images. For the first example, consider the 128 ×128 brain image in Fig 5a. the required view angle of projection φ_0 as well as the required lines of projections $p_{i,j}$ are defined by (12). Specifically, $\varphi_0 = \frac{\pi}{2} - \alpha$; *with* $\alpha = tan^{-1}$ (128), and the family of 128 ×128 = 16384 lines:

$$\begin{aligned} p_{i,j} &:= (j-1)\,cos\varphi_0 + (M-i+1)\,sin\varphi_0, \\ &\quad i = 1, 2 \ldots, 128, \quad j = 1, 2, \ldots, 128. \end{aligned}$$

Figure 5b shows the profile $f^{\vee}\left(p_{i,j}, \varphi_0\right)$, which is the raw data that assumed to be available. This graph consists of 16384 points.

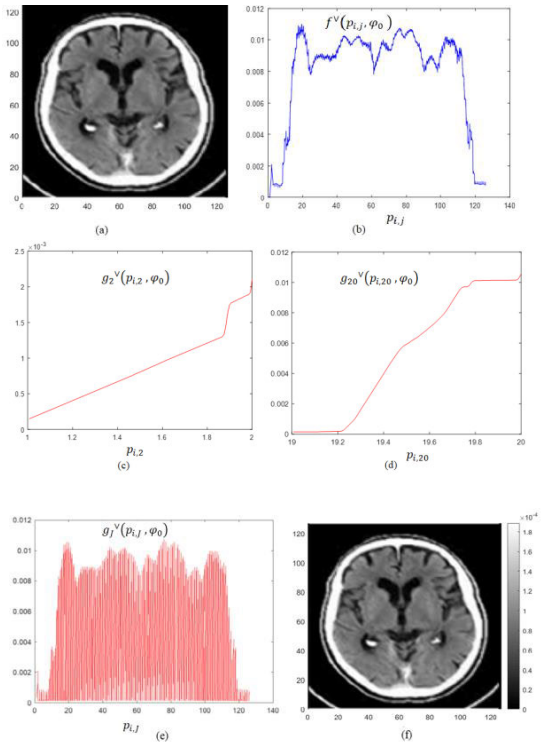

FIGURE 5. (a) Original image. (b) The required projections $f^{\vee}\left(p_{i,j},\varphi_0\right)$ at the one angle φ_0 and the lines $p_{i,j}$ from (12). (c-d) Two profiles $g_2^{\vee}\left(p_{i,2},\varphi_0\right)$ and $g_{20}^{\vee}\left(p_{i,20},\varphi_0\right)$. (e) $g_J^{\vee}\left(p_{i,J},\varphi_0\right)$ for all J. (f) The reconstructed image from (29) using the projections $g_J^{\vee}\left(p_{i,J},\varphi_0\right)$.

Now, observe that $g_J^{\vee}\left(p_{i,J},\varphi_0\right)$ in (29) is extracted from $f^{\vee}\left(p_{i,j},\varphi_0\right)$ as given in (18). Observe also that $g_J^{\vee}$ is calculated only for the lines $p_{i,J}, i = 1,2\ldots,M$. For instance, Fig. 5(c-d) show the projections $g_2^{\vee}\left(p_{i,2},\varphi_0\right)$ and $g_{20}^{\vee}\left(p_{i,20},\varphi_0\right), i. = 1,2\ldots,M$. Figure 5e shows $g_J^{\vee}\left(p_{i,J},\varphi_0\right)$ for all J and Fig. 5f displays the reconstructed image that was recovered column by column from left to right by solving (29), M times.

In addition to the visual comparisons between the original and reconstructed images; we use two quantitative measures:

The normalized average absolute distance,

$$D_1 = \frac{\sum\sum|F_{ij} - F_{ij}^*|}{\sum\sum F_{ij}} \tag{30}$$

And the root-mean-square error,

$$D_2 = \sqrt{\frac{\sum\sum[F_{ij} - F_{ij}^*]^2}{MN}} \tag{31}$$

where F_{ij} and F_{ij}^* represent the pixel values corresponding to the original image and the reconstructed image, respectively.

The values (30-31) for Fig. 5f are: $D_1 = 3.8 \times 0^{-14}$ and $D_2 = 9.5 \times 10^{-13}$. As observed, the reconstruction in Fig. 5f is exact. This is because of two factors: equation (8) that calculates the transform exactly, and equation (19) implemented in (29) that returns the image column by column precisely.

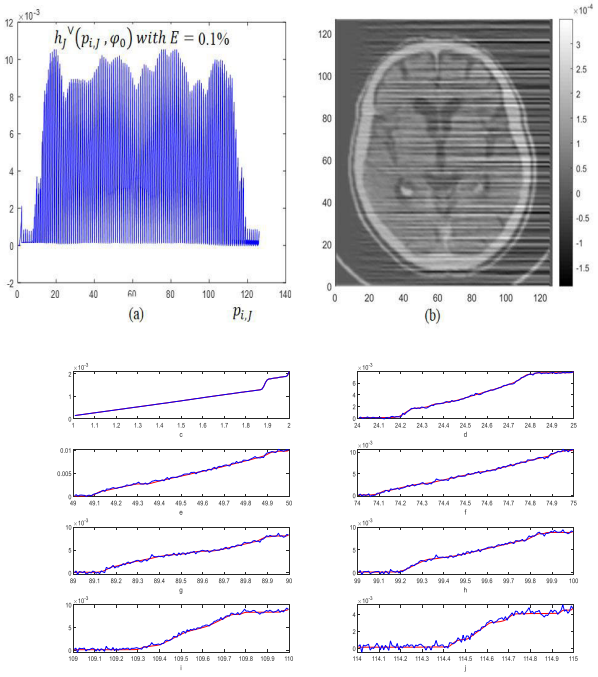

FIGURE 6. (a) The distorted $h_J^{\vee}\left(p_{i,J},\varphi_0\right)$ for all J. (b) The reconstructed image from (29) using the projections $h_J^{\vee}\left(p_{i,J},\varphi_0\right)$. (c-j) $h_J^{\vee}\left(p_{i,J},\varphi_0\right)$ -blue- versus $g_J^{\vee}\left(p_{i,J},\varphi_0\right)$ -red- for J = 2, 25, 50, 75, 90, 100, 110, and 115.

We now test the sensitivity of the proposed method under some perturbation of the Radon projections. Consider (29), assume that each of the original projections $f^{\vee}\left(p_{i,j},\varphi_0\right)$ is distorted, and is given by,

$$f_1^{\vee}\left(p_{i,j},\varphi_0\right) = (1+r)f^{\vee}\left(p_{i,j},\varphi_0\right) \tag{32}$$

for some small random number r in the range $-E \le r \le E$ with a choice of E.

For clarity of notation, we reserve $g_J^{\vee}$ from (18) when no noise is applied to $f^{\vee}\left(p_{i,j},\varphi_0\right)$, and we replace $g_J^{\vee}$ by $h_J^{\vee}$ when $f^{\vee}\left(p_{i,j},\varphi_0\right)$ is distorted by some r. So we have,

$$g_J^{\vee}(p,\varphi) = f^{\vee}(p,\varphi) - \sum_{i=1}^{M}\sum_{j=1}^{J-1} F_{ij}.B_{ij}^{\vee}(p,\varphi), \quad \mathrm{J} = 2,\ldots\mathrm{N}$$

and,

$$h_J^{\vee}(p,\varphi) = f_1^{\vee}(p,\varphi) - \sum_{i=1}^{M}\sum_{j=1}^{J-1} F_{ij}.B_{ij}^{\vee}(p,\varphi), \quad \mathrm{J} = 2,\ldots\mathrm{N} \tag{33}$$

Consider the above experiment on the brain image of Fig. 5a. Apply the distortion (32) on $f^{\vee}\left(p_{i,j},\varphi_0\right)$ with $E = 0.1\%$. The distorted $h^{\vee}\left(p_{i,J},\varphi_0\right)$ for all J is shown in Fig. 6a and the reconstructed image is shown in Fig 6b.The values (30-31) for Fig 6b are: $D_1 = .73$ and $D_2 = 0.15$.

Let us zoom in Fig 5e and Fig 6a. Fig 6 c-j show the plots $h^{\vee}\left(p_{i,J},\varphi_0\right)$; the blue graphs, against $g^{\vee}\left(p_{i,J},\varphi_0\right)$, the red graphs for the values $J = 2, 25, 50, 75, 90, 100, 110$, and 115.

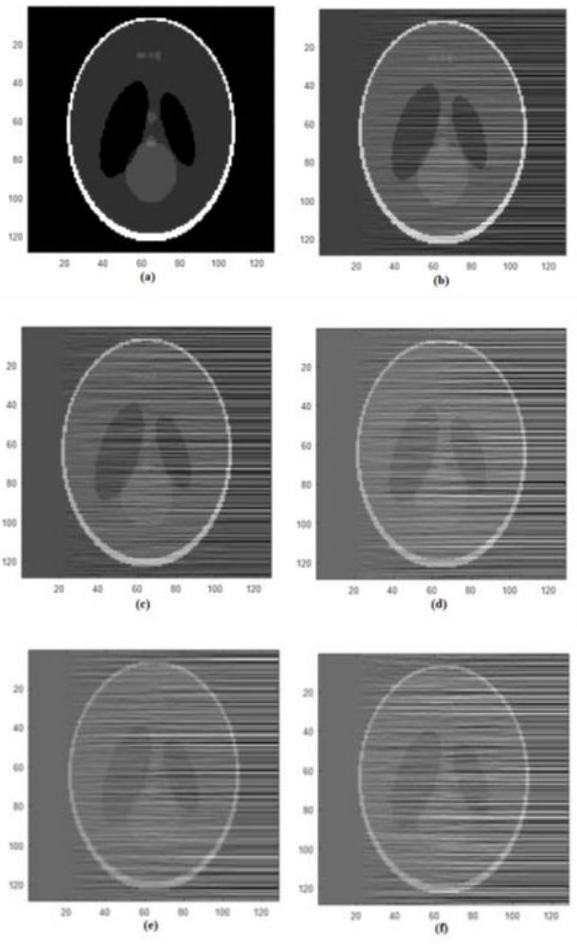

FIGURE 7. (a) Original image, (b-f) Reconstructed images correspond to perturbations of the Radon projections with a noise level of 0.1%, 0.2%, 0.3%, 0.4%, and 0.5%, respectively.

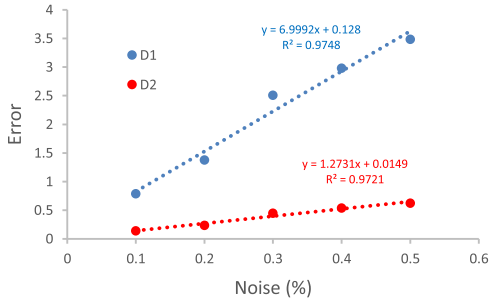

FIGURE 8. D_1 and D_2 errors plot for several levels of noise on projections for Shepp-Logan image.

For further testing, let us use 128 × 128 Shepp-Logan image with values of E range from 0.1% to 0.5%. Fig. 7 shows the visual results and table 1 displays the measures D_1 and D_2. In fact, Fig. 7b-6f are the reconstructed images after the perturbation of the Radon projections $f^{\vee}\left(p_{i,j}, \varphi_0\right)$ with a noise level 0.1%, 0.2%, 0.3%, 0.4%, and 0.5%, respectively.

From these experiments we observe the following:

First, with the absence of noise in $f^{\vee}\left(p_{i,j}, \varphi_0\right)$ the reconstruction is exact as in Fig 5f. As said, this accuracy

TABLE 1. Perturbation of data and error- D_1 and D_2.

E	D_1	D_2	Figure 7
0.1%	0.7866	0.1374	b
0.2%	1.3775	0.2373	c
0.3%	2.5095	0.4473	d
0.4%	2.9803	0.5392	e
0.5%	3.4848	0.6230	f

of reconstruction is due to equation (8) that calculates the transform exactly, and equation (19) implemented in (29) that returns the image column by column precisely.

Second, from Fig. 6b and Fig. 7b-f, the noise on any of these reconstructed images increases horizontally from left to right. That is due to the recursive nature of this method. We recover the image column by column, from left to right, and the error caused by the added noise accumulated. This observation can also be seen in the plots of Fig 6 c-j where a larger J means a larger deviation of the distorted projections $h^{\vee}\left(p_{i,J}, \varphi_0\right)$ from the exact projections $g^{\vee}\left(p_{i,J}, \varphi_0\right)$.

Third, from table 1, we see that the errors D_1 and D_2 increase linearly against the level of the added noise, this is suggested by Fig 8.

V. CONCLUSION

In this paper, we obtained two results; one is practical and the other is theoretical. Our practical result is described in equations (7) and (8) where it possible to compute the Radon transform of a given image precisely. For the second result, we have seen that a function of the form (7) can be reconstructed from its Radon transform using only one view angle with lines of projection described in equation (12). The approach can be categorized as an algebraic reconstruction, but it is merely a theoretical contribution for the field of limited data tomography.

REFERENCES

[1] J. Radon, "On the determination of functions from their integral values along certain manifolds," *IEEE Trans. Med. Imag.*, vol. MI-5, no. 4, pp. 170–176, Dec. 1986, doi: 10.1109/TMI.1986.4307775.

[2] S. R. Deans, *The Radon Transform and Some of Its Applications*. New York, NY, USA: Wiley, 1983.

[3] P. C. Hansen, J. Jørgensen, and W. R. Lionheart, *Computed Tomography: Algorithms, Insight, and Just Enough Theory*. Philadelphia, PA, USA: Society for Industrial and Applied Mathematics, 2021.

[4] G. N. Hounsfield, "Computerized transverse axial scanning (tomography): Part 1. Description of system," *Brit. J. Radiol.*, vol. 46, no. 552, pp. 1016–1022, 1973, doi: 10.1259/0007-1285-46-552-1016.

[5] C. L. Epstein, *Introduction to the Mathematics of Medical Imaging*. Upper Saddle River, NY, USA: Pearson Education, 2003.

[6] M. S. Jouini, F. Bouchaala, M. K. Riahi, M. Sassi, H. Abderrahmane, and F. Hjouj, "Multifractal analysis of reservoir rock samples using 3D X-Ray micro computed tomography images," *IEEE Access*, vol. 10, pp. 67898–67909, 2022, doi: 10.1109/ACCESS.2022.3186476.

[7] M. S. Jouini, F. Bouchaala, E. Ibrahim, and F. Hjouj, "Permeability and porosity upscaling method using machine learning and digital rock physics," in *Proc. 83rd EAGE Annu. Conf. Exhibit.*, 2022, pp. 1–5, doi: 10.3997/2214-4609.202210016.

[8] F. Hjouj and M. S. Jouini, "On the radon transform and linear transformations of images," in *Proc. 2nd Int. Conf. Digit. Med. Image Process.*, Nov. 2019, pp. 26–31, doi: 10.1145/3379299.3379306.

[9] F. I. Hjouj and M. S. Jouini, "On image registration using the radon transform: Review-and-improvement," in *Proc. 4th Int. Conf. Digit. Med. Image Process.*, Nov. 2021, pp. 17–23, doi: 10.1145/3506651.3506654.
[10] F. Hjouj, "Towards tomography with random orientation," in *Proc. 2nd Int. Conf. Digit. Med. Image Process.*, Nov. 2019, pp. 49–53, doi: 10.1145/3379299.3379309.
[11] G. Chen and S. Coulombe, "A new image registration method robust to noise," *Multidimensional Syst. Signal Process.*, vol. 25, no. 3, pp. 601–609, Jul. 2014.
[12] B. Xiao, J.-F. Ma, and J.-T. Cui, "Combined blur, translation, scale and rotation invariant image recognition by radon and pseudo-Fourier–Mellin transforms," *Pattern Recognit.*, vol. 45, no. 1, pp. 314–321, Jan. 2012.
[13] F. Hjouj and D. W. Kammler, "Identification of reflected, scaled, translated, and rotated objects from their radon projections," *IEEE Trans. Image Process.*, vol. 17, no. 3, pp. 301–310, Mar. 2008, doi: 10.1109/TIP.2007.916160.
[14] N. Chetih and Z. Messali, "Tomographic image reconstruction using filtered back projection (FBP) and algebraic reconstruction technique (ART)," in *Proc. 3rd Int. Conf. Control, Eng. Inf. Technol. (CEIT)*, May 2015, pp. 1–6, doi: 10.1109/CEIT.2015.7233031.
[15] M. Beister, D. Kolditz, and W. A. Kalender, "Iterative reconstruction methods in X-ray CT," *Phys. Medica*, vol. 28, no. 2, pp. 94–108, Apr. 2012, doi: 10.1016/j.ejmp.2012.01.003.
[16] K. J. Batenburg and L. Plantagie, "Fast approximation of algebraic reconstruction methods for tomography," *IEEE Trans. Image Process.*, vol. 21, no. 8, pp. 3648–3658, Aug. 2012.
[17] R. Gordon and G. T. Herman, "Algebraic reconstruction techniques (ART) for three-dimensional electron microscopy and X-ray photography," *J. Theor. Biol.*, vol. 29, no. 3, pp. 471–481, 1970.
[18] G. T. Herman and L. B. Meyer, "Algebraic reconstruction techniques can be made computationally efficient (positron emission tomography application)," *IEEE Trans. Med. Imag.*, vol. 12, no. 3, pp. 600–609, Sep. 1993, doi: 10.1109/42.241889.
[19] S. Kaczmarz, "Auflo sung von Systemen linearer gleichungen," *Bull Internat Acad PolonSci. Lettres A*, vol. 1937, Art. no. 335e57.
[20] T. Strohmer and R. Vershynin, "A randomized Kaczmarz algorithm with exponential convergence," *J. Fourier Anal. Appl.*, vol. 15, no. 2, pp. 262–278, Apr. 2009.
[21] D. Needell, N. Srebro, and R. Ward, "Stochastic gradient descent, weighted sampling, and the randomized Kaczmarz algorithm," *Math. Program.*, vol. 155, nos. 1–2, pp. 549–573, Jan. 2016, doi: 10.1007/s10107-015-0864-7.
[22] G. Wang, J. C. Ye, K. Mueller, and J. A. Fessler, "Image reconstruction is a new frontier of machine learning," *IEEE Trans. Med. Imag.*, vol. 37, no. 6, pp. 1289–1296, Jun. 2018, doi: 10.1109/TMI.2018.2833635.
[23] J.-Y. Lee, W. Kim, Y. Lee, J.-Y. Lee, E. Ko, and J.-H. Choi, "Unsupervised domain adaptation for low-dose computed tomography denoising," *IEEE Access*, vol. 10, pp. 126580–126592, 2022.
[24] Z. Qiao, X. Wen, X. Zhou, F. Qin, S. Liu, B. Gao, W. Liu, D. Chi, and Z. Liu, "Adaptive iterative guided filtering for suppressing background noise in ptychographical imaging," *Opt. Lasers Eng.*, vol. 160, Jan. 2023, Art. no. 107233.
[25] A. Benammar, A. Allag, R. Drai, M. Yahi, and T. Boutkedjirt, "Sinogram interpolation method for limited-angle tomography," in *Proc. Int. Conf. Adv. Electr. Eng. (ICAEE)*, Nov. 2019, pp. 1–5, doi: 10.1109/ICAEE47123.2019.9015130.
[26] J. Luo, W. Li, and Y. Zhu, "Reconstruction from limited-angle projections based on δ-u spectrum analysis," *IEEE Trans. Image Process.*, vol. 19, no. 1, pp. 131–140, Jan. 2010, doi: 10.1109/TIP.2009.2032893.
[27] Z. Hu, J. Gao, N. Zhang, Y. Yang, X. Liu, H. Zheng, and D. Liang, "An improved statistical iterative algorithm for sparse-view and limited-angle CT image reconstruction," *Sci. Rep.*, vol. 7, no. 1, pp. 1–9, Sep. 2017, doi: 10.1038/s41598-017-11222-z.
[28] F. Hjouj and M. S. Jouini, "Review and improvement of the finite moment problem," *Open Chem. Eng. J.*, vol. 14, no. 1, pp. 17–24, Apr. 2020, doi: 10.2174/1874123102014010017.
[29] H. Z. Shu, J. Zhou, G. G. Han, L. Luo, and J. J. Coatrieux, "Image reconstruction from limited range projections using orthogonal moments," *Pattern Recognit.*, vol. 40, no. 2, pp. 68–670, 2007, doi: 10.1145/3379299.3379309.
[30] X. B. Dai, H. Z. Shu, L. M. Luo, G. N. Han, and J. L. Coatrieux, "Reconstruction of tomographic images from limited range projections using discrete radon transform and tchebichef moments," *Pattern Recognit.*, vol. 43, no. 3, pp. 1152–1164, Mar. 2010.
[31] H. Qi, Z. Chen, S. Wu, Y. Xu, and L. Zhou, "Iterative image reconstruction using modified non-local means filtering for limited-angle computed tomography," *Phys. Medica*, vol. 32, no. 9, pp. 1041–1051, Sep. 2016.
[32] E. J. Candès, J. Romberg, and T. Tao, "Robust uncertainty principles: Exact signal reconstruction from highly incomplete frequency information," *IEEE Trans. Inf. Theory*, vol. 52, no. 2, pp. 489–509, Feb. 2006, doi: 10.1109/TIT.2005.862083.
[33] D. L. Donoho, "Compressed sensing," *IEEE Trans. Inf. Theory*, vol. 52, no. 4, pp. 1289–1306, Apr. 2006, doi: 10.1109/TIT.2006.871582.
[34] M. U. Ghani and W. C. Karl, "Deep learning-based sinogram completion for low-dose CT," in *Proc. IEEE 13th Image, Video, Multidimensional Signal Process. Workshop (IVMSP)*, Jun. 2018, pp. 1–5.
[35] X. Yang, M. Wolfman, D. Gursoy, and K. A. Katsaggelos. *Sinogram Image Completion for Limited Angle Tomography With Generative Adversarial Networks*. [Online]. Available: https://sigport.org/documents/sinogram-image-completion-limited-angle-tomography-generative-adversarial-networks
[36] A. Lucas, M. Iliadis, R. Molina, and A. K. Katsaggelos, "Using deep neural networks for inverse problems in imaging: Beyond analytical methods," *IEEE Trans. Signal Process. Mag.*, vol. 35, no. 1, pp. 20–36, Jan. 2018, doi: 10.1109/MSP.2017.2760358.
[37] J. Wang, L. Zeng, C. Wang, and Y. Guo, "ADMM-based deep reconstruction for limited-angle CT," *Phys. Med. Biol.*, vol. 64, no. 11, May 2019, Art. no. 115011, doi: 10.1088/1361-6560/ab1aba.
[38] H. Arjah, M. Hjouj, and F. Hjouj, "Low dose brain CT, comparative study with brain post processing algorithm," in *Proc. 2nd Int. Conf. Digit. Med. Image Process.*, Nov. 2019, pp. 1–7, doi: 10.1145/3379299.3379308.
[39] F. Natterer, *The Mathematics of Computerized Tomography*, vol. 32. SIAM, 2001, pp. 160–166.
[40] Z. Zhang and J. Bond, "A review of reconstruction methods for limited angle X-ray tomography in nondestructive evaluation applications," in *Review of Progress in Quantitative Nondestructive Evaluation*. 2019.
[41] S. Yoo, X. Yang, M. Wolfman, D. Gursoy, and A. K. Katsaggelos, "Sinogram image completion for limited angle tomography with generative adversarial networks," in *Proc. IEEE Int. Conf. Image Process. (ICIP)*, Sep. 2019, pp. 1252–1256, doi: 10.1109/ICIP.2019.8804416.

FAWAZ HJOUJ received the Ph.D. degree in mathematics from Southern Illinois University, USA, in 2004. He worked as an Assistant Professor with the Mathematics Department, East Carolina University, USA. In 2013, he joined the Petroleum Institute, United Arab Emirates, which became a part of the Khalifa University of Science and Technology. His research interests include Radon transformation that synthesizes numerical analysis and Fourier analysis, and computations on digital image processing with applications to different problems in the field of computerized tomography.

MOHAMED SOUFIANE JOUINI received the master's degree in electrical engineering and the M.Sc. degree in signal and image processing from the National Polytechnic Institute of Toulouse, and the Ph.D. degree in signal and image processing from Bordeaux University. He had several positions in Research and Development centers in industry. He was a Research Scientist of digital rock physics at the Total E and P Research Center, PAU, France, from 2006 to 2009. He was appointed as a Research and Development Engineer of image processing algorithms for security applications at the SAGEM SECURITE (IDEMIA) Research and Development Center, Paris, France. In January 2010, he was hired as a Research and Teaching Associate at ADNOC (Petroleum Institute) to work on projects in digital rock physics. In 2014, he joined as an Assistant Professor at the Mathematics Department, Khalifa University, where he is currently an Associate Professor, experienced in numerical simulations to model rock properties based on X-Ray computed tomography images.